PHYSICAL REVIEW B VOLUME 44, NUMBER 24 15 DECEMBER 1991-II

Electron states, magnetism, and the Verwey transition in magnetite

Ze Zhang and Sashi Satpathy
Department of Physics & Astronomy, University of Missouri–Columbia, Columbia, Missouri 65211

(Received 18 March 1991)

Using density-functional calculations, we examine the electronic structure of magnetite in the spinel crystal structure in order to gain insight into the nature of the Verwey transition. The calculated cohesive and magnetic properties are in agreement with experimental results. The magnetic structure is analyzed using a Stoner model as well as from calculations within the framework of the local-spin-density approximation to the density-functional theory. The calculations show a minority-spin band at the Fermi energy consisting of t_{2g} orbitals on the Fe(B) sublattice. These results suggest a three-band spinless model Hamiltonian for the description of the Verwey transition. The hopping integrals and the electron interaction parameters entering the model Hamiltonian are calculated using the "constrained" density-functional theory. The calculated parameters are consistent with the electronic origin of the Verwey transition.

I. INTRODUCTION

Solids with strong electron correlation exhibit many interesting physical phenomena and encompass one of the lively areas of research in condensed matter physics.[1] Some examples on which considerable attention has been focused in the recent past are the heavy-fermion systems, the transition-metal oxide Mott insulators, the high-T_c superconductors, and systems such as magnetite exhibiting the peculiar Verwey metal-insulator transition, to name a few. The nature of electron states in these systems and how electronic correlation manifests itself in various physical phenomena that they exhibit are issues of fundamental importance. In this paper we focus on magnetite and examine the nature of the electron states as a first step towards the understanding of the Verwey metal-insulator transition.

The Verwey transition in magnetite is a peculiar metal-insulator transition that has been studied for quite some time.[2] This is a first-order transition and is characterized by an abrupt decrease in conductivity by two orders of magnitude below the Verwey temperature of $T_V \sim 120$ K.[3] From the outset, the Verwey transition has been interpreted as an order-disorder transition of the Fe^{2+} and Fe^{3+} ions which arrange on the "so-called" B sublattice of the spinel structure. The Fe^{2+} ion may be viewed as an "extra" electron plus an Fe^{3+} ion with the "extra" electrons interacting via a repulsive Coulomb interaction.

Quite early on Anderson[4] pointed out the remarkable property of this sublattice that the short-range part of the Coulomb interaction is minimized by $\sim(\frac{3}{2})^{N/2}$ different configurations of the ions where N is the number of B sites. Only a few of these configurations have long-range order (LRO) as well. Anderson interpreted the Verwey transition as a loss of the LRO of the "extra" electrons on the B sublattice at temperature above T_V while the short-range order (SRO) is maintained across the transition. This interpretation is consistent with the observed entropy change at the transition ($0.3kN$) (Ref. 5) which is decisively smaller than the entropy change ($0.7kN$) corresponding to a total loss of order above T_V. Experiments indeed indicate the presence of LRO at temperature below T_V, however, the LRO seems to be much more complicated than the simple Verwey[3] order where the ions are ordered in alternate (001) planes of Fe^{2+} and Fe^{3+}. To date the exact ordering of the ions below T_V is not precisely known even though recently significant progress has been made in this direction.[6]

Another area we will have to consider is the magnetic structure of magnetite and its possible relationship to the Verwey transition. The magnetic properties of magnetite are by themselves quite interesting.[7] Discovered around 1500 B.C., it is the earliest known magnet. A large number of magnetic materials have been discovered since then; nevertheless magnetite remains one of the extensively used magnetic materials for industrial applications, notably in computer memory cores and in magnetic recording.

Several models have been proposed to describe the mechanism of electrical conduction in magnetite and its behavior near the Verwey transition. Cullen and Callen[8] have proposed a simple model in which the "extra" electrons on the B sublattice move in a nondegenerate spinless band. Such a model has two parameters, viz., the tight-binding hopping integral t related to the bandwidth of the "extra" electrons and the nearest-neighbor Coulomb repulsion U_1. Cullen and Callen estimated using their model that if the condition $U_1/t \gtrsim 2.5$ is true then the material is metallic and for larger values of this parameter a charge ordering similar to a Wigner transition occurs, resulting in an insulator. On the other hand, isotope substitution experiments[9] seem to propose that electron-phonon coupling, leading possibly to polaron formation, might play some role in the Verwey transition. Yamada[10] and Chakraverty[11] in fact favor the picture of molecular polarons or bipolarons. According to Yamada's molecular polaron picture, the Verwey transition is viewed as a cooperative ordering of the molecular polarons presumed to interact via the strain fields that they generate. One picture[12] would then be that above

T_V a "Wigner glass" of bipolarons is formed, some of which dissociate and result in conduction as temperature is raised, presumably by nearest-neighbor hopping. Considering the complexity of the problem, it is difficult to choose among the various mechanisms for the metal-insulator transition.

Lately it has become possible to derive the electron interaction and hopping parameters from first-principles local-density calculations. Knowledge of the magnitudes of these quantities is important to differentiate the applicability of various models to the Verwey transition and is a first step towards an understanding of the metal-insulator transition in this system. In this paper our primary goal is to study the nature of the electron states and calculate the interaction parameters. Based on our results we propose a three-band electronic Hamiltonian for the motion of the "extra" electrons on the B sublattice of the spinel structure.

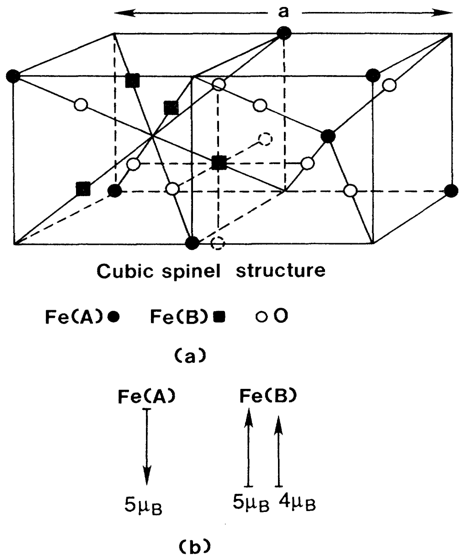

FIG. 1. Cubic spinel crystal structure. The crystal is made up of alternate stacking of the two cubes which form the basis in a face-centered-cubic (fcc) lattice. In magnetite the magnetic moments on the two Fe A and B sublattices are aligned *ferrimagnetically* (b). The A sublattice consists of Fe^{3+} atoms while the B sublattice consists of an equal number of Fe^{3+} and Fe^{2+} atoms resulting in the "inverse" spinel crystal structure.

II. CRYSTAL STRUCTURE

Magnetite (Fe_3O_4) is typical of a class of materials called ferrites forming in the spinel crystal structure (space group $Fd3m$) or in closely related structures. The spinel structure can be conveniently thought of as made up by alternate stacking of two different cubes as shown in Fig. 1. The large oxygen atoms form a close-packed face-centered-cubic structure with the smaller iron atoms occupying the interstitial positions. There are two types of interstitial sites both occupied by the iron atoms: the tetrahedral (8a) (Ref. 13) or A sites, and the octahedral (16d) or the B sites. The Bravais lattice is face-centered cubic (fcc) with two formula units (14 atoms) in the unit cell. The valence of various atoms is described by the formal chemical formula, $Fe^{3+}(Fe^{3+}Fe^{2+})(O^{2-})_4$. The Fe^{3+} ions occur on the A sublattice while the B sublattice contains a mixture of Fe^{3+} and Fe^{2+}, leading to the so-called "inverse" spinel structure. Below the Verwey transition temperature there is a small change in the crystal structure which becomes monoclinic.[6]

The intrinsic magnetization of magnetite can be explained by assuming that the magnetic moments within the A and the B sublattices are ferromagnetically aligned while the two sublattices are antiferromagnetic with respect to each other, and further by assigning, on the basis of Hund's rules, the magnetic moments of $5\mu_B$ and $4\mu_B$ to the Fe^{3+} and the Fe^{2+} ions, respectively. This magnetic structure, indicated in Fig. 1, was first proposed by Néel[14] to explain the magnetization data and was subsequently established by Shull, Wollan, and Koehler[15] from neutron scattering experiments.

The band calculations reported here were performed using the local-spin-density approximation (LSDA) to the density-functional theory and the "constrained" density-functional methods. The self-consistent linear muffin-tin orbitals method in the atomic spheres approximation (LMTO-ASA) was used.[16] We used the von Barth–Hedin exchange-correlation potentials.[17] In addition to the 14 atoms in the unit cell, we included 18 empty spheres. Their positions and the sphere radii used in our calculations are given in Table I. Electrons up to and including Fe($3p$) and O($1s$) orbitals were treated as frozen core electrons. In the basis set, only the muffin-tin orbitals of angular momentum s, p, and d on the Fe and

TABLE I. Atom positions and sphere sizes for the LMTO calculations of Fe_3O_4.

Atom	Core	Site index	Muffin-tin-sphere radius (Å)
Fe (A site)	[Ar]	8a	0.95
Fe (B site)	[Ar]	16d	1.15
O	[He]	32e ($x=0.379$)	1.20
$E(1)$		16c	1.12
$E(2)$		8b	0.80
$E(3)$		48 f ($x=0.25$)	0.84
Lattice constant	$a=8.396$ Å		

O atoms, and *s*, *p* orbitals on the empty spheres were retained. The one-electron densities of states were calculated with 56 **k** points in the irreducible Brillouin zone (BZ). The "constrained" LDA method will be sketched in a later section.

III. NON-SPIN-POLARIZED LDA BANDS AND BAND MAGNETISM WITHIN THE STONER MODEL

Before we present results of the spin-polarized LSDA calculation, it is instructive to examine the salient features of the results of the non-spin-polarized LDA calculation. The LDA bands as well as the one-electron density of states (DOS) are shown in Fig. 2. A key feature is that the O(2*p*) bands occur well below the Fermi energy which lies in the middle of the Fe(3*d*) bands. Since the position of the O(2*p*) bands is expected to remain more or less unaffected as a result of spin polarization of the Fe(3*d*) bands occurring at the Fermi energy, the important bands are the Fe(3*d*) bands for transport properties such as conductivity with the O(2*p*) bands playing minor roles. The density of states at the Fermi energy is rather high, about 40±5 states/eV cell, indicating a ferromagnetic instability within the Stoner model consistent with the magnetic nature of the compound.

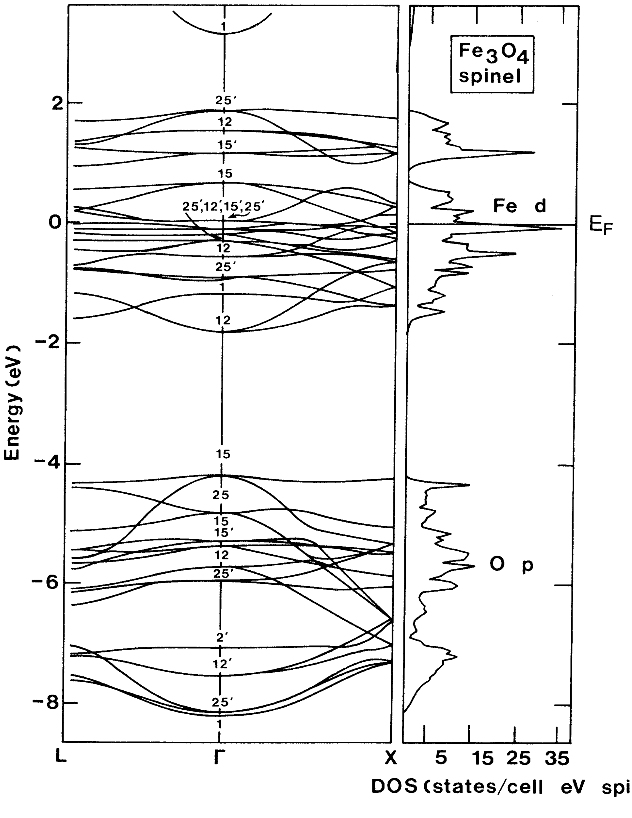

FIG. 2. Non-spin-polarized electron band structure and the density of states obtained from local-density LMTO calculation.

The Stoner model[18] has been successfully applied to describe the ferromagnetism of the 3*d* transition metals. Part of the reason for the success of the Stoner model when used in conjunction with nonmagnetic, local-density calculations is due to the fact that the local-spin-density theory reduces to an effective Stoner model within the first-order perturbation approximation.[19–21] Recently the model has been applied to describe successfully the detailed magnetic behavior of iron.[22] As mentioned earlier, in magnetite the magnetic moments of the iron atoms are aligned ferromagnetically in each of the Fe(*A*) and Fe(*B*) sublattices while the two sublattices are aligned in the opposite direction. Below we apply the Stoner model to each of the two individual sublattices separately, justification for which will be given below.

Within the Stoner model, magnetism is the result of competition between two energies: (i) increase in the kinetic energy as electrons are forced to occupy the higher bands and (ii) reduction in the "exchange" energy which is a reduction of the Coulomb repulsion brought about via the Pauli exclusion principle. For a given magnetization per atom, m, the net energy is given by the well-known[23] expression

$$E(m)=\frac{1}{2}\int_0^m \frac{m}{\bar{N}(n,m)}\,dm-\tfrac{1}{4}Im^2 , \tag{1}$$

where I is the Stoner exchange parameter and $\bar{N}(n,m)$ is the electron density of states per atom spin averaged over the band energy range ε_+ and ε_-, which are the Fermi energies corresponding to the occupancy of $n/2\pm m/2$ states per atom spin:

$$\bar{N}(n,m)=m/(\varepsilon_+-\varepsilon_-) .$$

A ferromagnetic solution with net magnetization m_0 is given by the condition that the expression for energy (1) is a minimum, i.e., $dE(m)/dm|_{m_0}=0$, which leads to the Stoner condition,

$$I\bar{N}(n,m_0)=1 . \tag{2}$$

The solution is stable if the second derivative of the energy with respect to the magnetization is negative, i.e., $d^2E(m)/dm^2|_{m_0}<0$, leading to the condition

$$d\bar{N}(n,m)/dm|_{m=m_0}<0 . \tag{3}$$

If the condition (3) is not satisfied, then the magnetic solution is metastable.

The Stoner condition (2) may also be derived by equating the chemical potentials μ_+ and μ_- for the up and the down spins. The chemical potentials, defined as the energy needed to add or remove an electron from the respective spin band, are given by

$$\mu_\sigma=\varepsilon_\sigma+In_{-\sigma} , \tag{4}$$

where σ denotes the two spins and $n_\pm=(n/2\pm m/2)$. The exchange part favors addition of the extra electron to the majority band in accord with Hund's rules for isolated atoms. Equating the two chemical potentials one obtains the Stoner condition (2).

We now extend the Stoner model to the two coupled sublattices in magnetite and we will show that to a very good approximation one can treat the two sublattices independently. Since in establishing magnetic equilibrium electrons can now shift between the two spin bands and between the two sublattices (although we will argue that the latter is small in general), we must include the variation of the effective on-site energies with the number of *d* electrons caused by the on-site Coulomb interaction. Thus the expression for the chemical potential for the *A* site is given by

$$\mu_\pm^A=\varepsilon_\pm(n_A^0,m_A)+U_A(n_A-n_A^0)+I_A\frac{n_A\mp m_A}{2} \tag{5}$$

with a similar expression holding for the *B* sites. Here, n_A^0 (n_A) is the total number of *d* electrons on an *A*-sublattice atom before (after) magnetic polarization was allowed. Since electrons can shift between the *A* and *B* sublattices following magnetic polarization, the quantities n_A and n_A^0 can be different. The second term in (5) accounts for the shift of the on-site energy because of the Coulomb interaction U_A. Equating the two chemical potentials in (5) to each other and to the chemical potentials on the *B* sublattice, we now get the Stoner conditions for the two sublattices:

$$I_A\bar{N}(m_A,n_A)=1 \ , \tag{6}$$

$$I_B\bar{N}(m_B,n_B)=1 \ , \tag{7}$$

and

$$\varepsilon_+^A+\varepsilon_-^A+2U_A(n_A-n_A^0)+I_An_A =\varepsilon_+^B+\varepsilon_-^B+2U_B(n_B-n_B^0)+I_Bn_B \ . \tag{8}$$

Additionally, since the total number of electrons remains unchanged as a result of magnetic polarization, we have the condition

$$n_A+2n_B=n_A^0+2n_B^0 \ . \tag{9}$$

The factors of 2 in Eq. (9) arise since the Fe(*B*) sublattice contains twice as many atoms as the Fe(*A*) sublattice. Notice that since Eq. (5) does not contain any exchange interaction between the *A* and *B* atoms, the relative orientation of the magnetic moments between the two sublattices is *not* predicted.

In general, Eqs. (6)–(9) have to be solved self-consistently for the number of electrons, n_A, n_B, and the magnetization, m_A, m_B, of the two sublattices. However, in Eq. (8) since *U* is by far the largest of all energies involved, we must have

$$n_A\approx n_A^0 \quad \text{and} \quad n_B\approx n_B^0 \ , \tag{10}$$

which follows from Eqs. (8) and (9) and is in fact verified from the results of our LSDA calculations. This is a statement that in a localized picture the electrons, when given the degree of freedom to spin polarize, do not shift appreciably between the atoms in the solid. The Coulomb energy cost for this is too high. Rather, they redistribute between the two spin states on the same atom. The basic point here is that the number of electrons on various atoms is controlled to a large extent by the Coulomb *U* and is not affected significantly by spin polarization. Thus we only need to satisfy the two equations (6) and (7) with n_A, n_B replaced by n_A^0, n_B^0 as indicated from (10). The net result is that we have to fulfill the Stoner conditions for the individual sublattices with the average DOS $\bar{N}$ calculated from the non-spin-polarized LDA results.

In Fig. 3 we show the graphical solution of the Stoner equations for the two iron sublattices in magnetite. The inputs needed are the Stoner parameter *I* as well as the one-electron *d* orbital DOS obtained from the LDA calculation. The *d*-orbital DOS for the individual sublattices is shown in the left side of Fig. 3, from which one

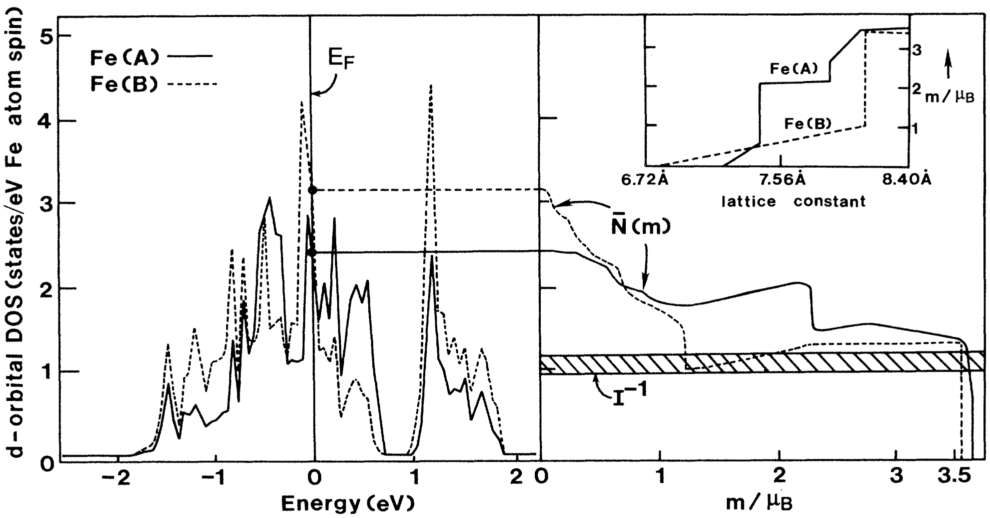

FIG. 3. Stoner analysis of the band magnetism of Fe(*A*) and Fe(*B*) sublattices following Eqs. (6), (7), and (10). Inset shows the predicted decrease of the sublattice magnetic moments with lattice compression.

can easily compute $\bar{N}(m)$. By definition $\bar{N}(m=0)$ equals the d orbital DOS at the Fermi energy as seen in Fig. 3. The Stoner parameter I can be calculated in the LSDA. In bcc Fe, the value of I is ~65 mRy as calculated by Poulsen, Kollár, and Andersen[24] and ~68 mRy as calculated by Janak.[21] Considering the spirit of the Stoner approach and the fact that our results of the Stoner analysis are rather insensitive to small changes in I, we have taken the value of I to be in the range 60–80 mRy. From the graphical solution we find a magnetization of $\approx 3.5\mu_B$ for both A and B sublattices. We also notice from Fig. 3 that for the B sublattice there is another stable solution with $m \approx 1.2\mu_B$ but this solution appears to have a slightly higher energy.

The inset in Fig. 3 shows the results of our Stoner analysis concerning how the magnetization would change if we compress the lattice. The value of the Stoner parameter is expected to increase somewhat when the lattice is compressed. In fact a simple derivation by Bloch[25] shows that for the jellium model $I \propto V^{-1/3}$. From a realistic calculation of the Stoner parameter for bcc iron by Krasko[22] it is seen that the Stoner parameter does indeed increase with lattice compression roughly following the Bloch expression. We have, however, neglected the small volume dependence of the value for the Stoner parameter I and further we have assumed the bandwidth to be inversely proportional to the fifth power of the distance between Fe atoms, which is how the hopping integrals between d orbitals fall off. With compression of the lattice the bandwidth becomes progressively broader, which results in a gradual reduction of the magnetic moment as seen from Fig. 3.

TABLE II. Cohesive properties of Fe_3O_4 from LSDA calculation.

	Lattice constant	Cohesive energy	Bulk modulus
Theory	8.397 Å	−33 eV/cell	2.1 Mbar
Expt.	8.394 Å	−29.56 eV/cell	

IV. LOCAL-SPIN-DENSITY CALCULATION

In this section we present the results of our local-spin-density calculation of the electron bands of Fe_3O_4. The cohesive properties of Fe_3O_4 as obtained from the LSDA calculation are shown in Table II. Both the lattice constant as well as the cohesive energy agree very well with the respective experimental values. In Fig. 4 we show the electron bands obtained from the LSDA calculation and Fig. 5 shows the spin-projected densities of states. Like in the non-spin-polarized calculation we find the O(p) orbitals to lie well below the Fermi energy, with the electron bands near the Fermi energy consisting primarily of Fe(d) orbitals. The results of our spin-polarized calculations generally agree with the earlier augmented plane wave (APW) calculations of Yanase and Siratori.[26]

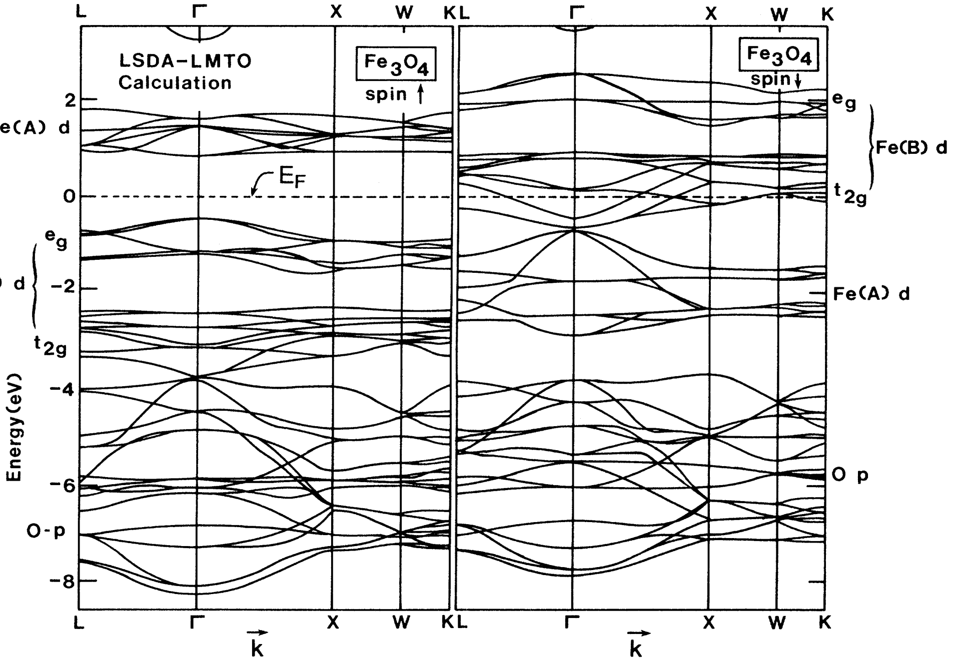

FIG. 4. Spin-polarized electron bands obtained from the local-spin-density LMTO calculation. Only minority-spin (spin-↓) electrons are present at the Fermi energy.

TABLE III. Calculated spin moments on various atoms in Fe_3O_4.

Atom	Atomic number	Charge	Spin moment (μ_B)	
Fe(A)	26	23.52	-3.46	($\times 2$)
Fe(B)	26	24.24	$+3.57$	($\times 4$)
O	8	8.75	$+0.10$	($\times 8$)
E spheres	0	0.33	-0.01	($\times 18$)
Total	220	220	8.00/Fe_6O_8	

As indicated from Fig. 5, the exchange splitting Δ_{ex} between the spin-up and -down d electrons on the Fe atom is roughly 3.5 eV. This is consistent with the photoemission spectra of Bishop and Kemeny[27] where the separation between the minority- and the majority-spin peaks is 3–4 eV. In addition to the exchange splitting, the fivefold d levels are split into t_{2g} and e_g orbitals by the crystal field. The crystal-field splitting Δ_{CF}, generated because of differences in covalent mixing and electrostatic interaction with neighboring atoms, is approximately 2 eV for the Fe(B) atom while it is less than a few tenths of an eV for the Fe(A) atom. This difference may be attributed to the large covalent mixing of the Fe(B) orbitals with its six nearest neighbors of the same kind.

The calculated spin moments on various atoms are shown in Table III. The calculated net magnetic moment is $4.0\mu_B/Fe_3O_4$ formula unit compared to the experimental value of 4.1 units.[28,29] The magnitudes of the magnetic moments on the individual Fe(A) and Fe(B) sites are roughly $3.5\mu_B$ in agreement with the results of the Stoner analysis of the previous section. The magnetic moment on an atom in a solid is of course an ill-defined quantity as charge cannot be unambiguously partitioned to be belonging to a certain atom. Thus the magnetic moment on individual atoms would depend on the choice of the muffin-tin radii. It is nevertheless interesting to point out the measurement of the magnetic form factor using the polarized neutron diffraction which indicates a moment of $3.82\mu_B$ for the A site.[30] This value is very different from the value of $5\mu_B$ obtained from Hund's rules and using the nominal Fe^{3+} charge for the ion atom on the A site indicating the itinerant nature of magnetism in magnetite. The high-spin state of the Fe atoms is consistent with the argument[31] that a high-spin state is indicated if the exchange splitting Δ_{ex} is greater than the crystal-field splitting Δ_{CF}. Additionally, we find that the magnetic moments on the A and the B sublattices are antiferromagnetically aligned consistent with experiment. We find the charge distribution to be consistent with the rough chemical formula of $Fe(A)^{3+}[Fe(B)^{2.5+}]_2O_4^{2-}$.

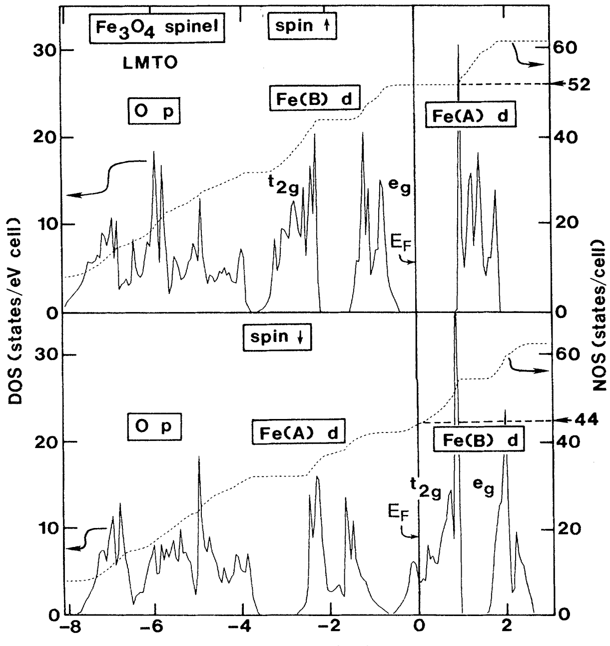

FIG. 5. Spin-projected one-electron densities of states and numbers of states for magnetite. The calculation predicts a net magnetic moment of $8.0\mu_B$ per unit cell which consists of two formula units.

A remarkable feature of the spin-polarized bands (Figs. 4 and 5) is that the spin-↑ bands (majority spins) are semiconducting while the spin-↓ bands (minority spins) are metallic. Only spin-↓ electrons are present at the Fermi energy and, moreover, these electrons have predominantly Fe(B) character. The spin-↓ character of the Fermi-energy electrons is in agreement with the earlier APW calculations of Yanase and Siratori[26] as well as with the spin-polarized photoemission experiments of Alvarado *et al.*[32] In this experiment, predominantly spin-↓ electrons were photoemitted from Fe_3O_4 at the photon energy corresponding to the photoelectric threshold consistent with the key feature of the LSDA bands at the Fermi energy. The fact that the observed spin polarization in Ref. 32 at the photoelectric threshold is less than 100% may be ascribed to experimental difficulties such as complications introduced by surface effects on the magnetic structure as the photoelectric probing depth is typically only a few atomic layers. Furthermore, collision processes could induce spin flips before the electron is photoemitted out of the sample.

V. ELECTRON BANDS NEAR FERMI ENERGY: MODEL ELECTRONIC HAMILTONIAN

Since electrons near the Fermi energy are important for the transport properties we examine the nature of the

TABLE IV. Wave-function characters of the minority-spin (↓) bands near Fermi energy at the Γ point.

			Orbital contribution to the charge density (%)			
Symmetry	Degeneracy	Energy[a] (eV)	Fe(*A*) total	Fe(*B*) $s+p,d$	O total	Empty total
$\Gamma_{25'}$	3	0.9	0	1,92	5	2
$\Gamma_{15'}$	3	0.8	0	0,98	0	2
$\Gamma_{25'}$	3	0.15	2	0,88	6	4
Γ_{1}	1	−0.44	2	1,75	14	8
Γ_{12}	2	−0.65	12	0,67	12	9

[a] Energy eigenvalues are with respect to the Fermi energy.

electron bands near the Fermi energy in some detail and propose a simple model Hamiltonian which, we believe, contains the key physics of the metal-insulator transition.

As discussed earlier only spin-↓ bands (minority spins) are present near the Fermi energy. The bands, about 1.55 eV wide, are shown in Fig. 6 and have the predominant contribution from *d* orbitals of the Fe(*B*) atoms as seen from the wave-function characters at the Γ point (see Table IV). In fact the bands consist primarily of the t_{2g} (*xy*, *yz*, and *zx*) orbitals centered on the Fe(*B*) atoms as is clear from the following discussions. There is exactly half an electron per Fe(*B*) atom (in total two per unit cell) occupying these t_{2g} bands.

In total there are twelve t_{2g} orbitals since we have four Fe(*B*) atoms per unit cell. As seen from Table V these orbitals span the $\Gamma_1+\Gamma_{12}+\Gamma_{15'}+2\Gamma_{25'}$ irreducible representations of the O_h point group which is the appropriate group at the Γ point for the spinel structure. This symmetry combination is consistent with the symmetries of the calculated spin-↓ bands shown in Fig. 6. Confirmation of the predominant participation of the t_{2g} orbitals is seen from the right part of Fig. 6 where we have projected out the contribution of the Fe(*B*) t_{2g} orbitals to the total density of states from which we find that the t_{2g} orbitals have about 90% contribution to the total DOS. It is therefore clear that these orbitals will dominate electrical conduction and other transport properties. We may point out here that the electron bands near Fermi energy are similar to those in the $LiTi_2O_4$ spinel compound, except that there states with *both* spins occur at E_F.[33]

At the *B* site in the spinel structure the crystal field is trigonal which causes the five *d* orbitals to split into two doublets (e_g) and one singlet (a_{1g}). The octahedral component of the crystal field at the *B* site is strong enough that the t_{2g} (*xy*, *yz*, and *zx*) and e_g (x^2-y^2 and $3z^2-1$) orbitals originating from the five *d* orbitals form two separate and nonoverlapping bands. The t_{2g} orbitals further split into a_{1g} and e_g symmetry combination by the trigonal component of the crystal field to produce the overall $2e_g+a_{1g}$ splitting. However, for the present compound the $a_{1g}-e_g$ splitting of the t_{2g} band is negligible in comparison with its width. This may be seen, for instance, by examining the bands at the Γ point at which the singlet a_{1g} level spans the $\Gamma_1+\Gamma_{25'}$ representations. As seen from Fig. 6 there are two states of $\Gamma_{25'}$ symmetry; of these the one with the higher energy and the Γ_1 state are made out of the a_{1g} orbitals. From the Γ-point energies it is clear that the average of the energies of the a_{1g}-derived orbitals is roughly the same as the average of the rest, which are the e_g-derived orbitals.

This is in contrast to the key assumption that Cullen and Callen had made[34] in proposing the one-band model Hamiltonian, where it was assumed that the "extra" electron moves in the a_{1g} band split off below the rest of the *d* bands of other symmetries. Rather we propose from our above results a model Hamiltonian similar to the Cullen-Callen Hamiltonian, but one where the "extra" electrons move in a three-band Hamiltonian formed by the t_{2g} (*xy*, *yz*, and *zx*) orbitals on the *B* sublattice:

$$H=\sum_{i,j}\sum_{\mu,\nu=1}^{3} t_{\mu\nu}a^{\dagger}_{i\mu}a_{j\nu}+\sum_{i,j}\sum_{\mu,\nu=1}^{3} U_{i\mu,j\nu}n_{i\mu}n_{j\nu}\ . \qquad (11)$$

Here μ and ν denote the three orbitals *xy*, *yz*, or *zx* and *i*

TABLE V. Irreducible representations of the O_h point group spanned by selected atomic orbitals in Fe_3O_4 at the Γ point.

Atomic orbitals	Number of orbitals per unit cell of each spin	Irreducible representations
Fe(*A*)*d*	2×5	$\Gamma_{12}+\Gamma_{15}+\Gamma_{12'}+\Gamma_{25'}$
Fe(*B*)t_{2g}	4×3	$\Gamma_1+\Gamma_{12}+\Gamma_{15'}+2\Gamma_{25'}$
Fe(*B*)e_g	4×2	$\Gamma_{12}+\Gamma_{15'}+\Gamma_{25'}$
Fe(*B*)a_{1g}	4×1	$\Gamma_1+\Gamma_{25'}$
O(*p*)	8×3	$\Gamma_1+\Gamma_{12}+2\Gamma_{15}+\Gamma_{25}$ $+\Gamma_{2'}+\Gamma_{12'}+\Gamma_{15'}+2\Gamma_{25'}$

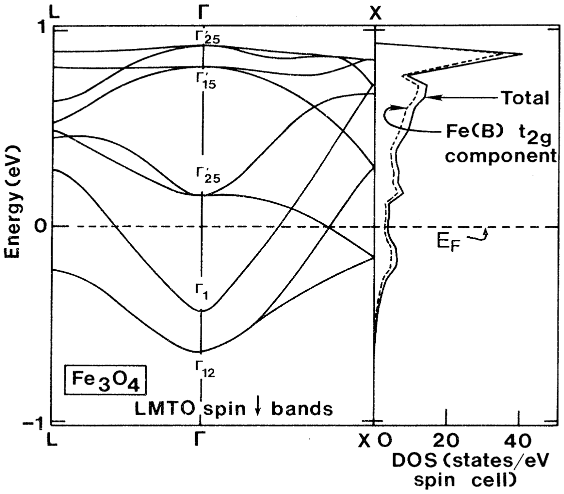

FIG. 6. Details of the minority electron bands near Fermi energy. Right part of the figure shows the total DOS and the partial DOS corresponding to the t_{2g} orbitals of the Fe atom on the B sublattice.

and j are the site indices on the B sublattice. The first term in (11) is the near-neighbor hopping term and the second term is the Coulomb interaction term. The parameters of the three-band Hamiltonian (11) are estimated in the next two sections.

VI. CALCULATION OF HOPPING INTEGRALS

We now calculate the hopping integrals in a simple tight-binding model where we retain only the t_{2g} orbitals on the Fe(B) atoms and in addition only the nearest-neighbor interactions between these orbitals. Furthermore, since the $a_{1g}-e_g$ splitting caused by the trigonal crystal field is small, in the following tight-binding fit we ignore this small splitting so that the on-site energies of the three orbitals are taken to be equal. We choose the tight-binding parameters by fitting the LMTO bands near the Fermi energy, Fig. 6, from the procedure sketched below.

The Bloch function $|\lambda\mathbf{k}\rangle$ may be expanded in terms of the 12 t_{2g} orbitals per unit cell denoted by $|\mathbf{R},n\rangle$:

$$|\lambda\mathbf{k}\rangle=\sum_{\mathbf{R}} e^{i\mathbf{k}\cdot\mathbf{R}}\sum_{n} b_n^{\lambda\mathbf{k}} e^{i\mathbf{k}\cdot\tau_n}|\mathbf{R}n\rangle \ . \tag{12}$$

Here $\mathbf{R}$ denotes the unit cell, n denotes the 12 orbitals in the basis set, τ_n is the position of the basis atom on which the nth orbital is located, λ is the band index, and $\mathbf{k}$ is the Bloch momentum. For the Bloch function (12) to be an eigenfunction, the coefficients $b_n^{\lambda\mathbf{k}}$ must satisfy the standard eigenvalue equation

$$\sum_n H_{mn}(\mathbf{k})b_n^{\lambda\mathbf{k}}=E(\lambda\mathbf{k})b_m^{\lambda\mathbf{k}} \ , \tag{13}$$

where

$$H_{mn}(\mathbf{k})=\sum_{\mathbf{R}} e^{i\mathbf{k}\cdot(\mathbf{R}+\tau_n-\tau_m)}\langle 0m|H|\mathbf{R}n\rangle \ . \tag{14}$$

Here $\langle 0m|H|\mathbf{R}n\rangle$ are the hopping integrals between the localized orbitals. Since we retain only the nearest-neighbor matrix elements in our tight-binding fit, apart from the onsite matrix element which merely serves to redefine the zero of energy, we have only three independent dd matrix elements, viz., $t_{dd\sigma}$, $t_{dd\pi}$, and $t_{dd\delta}$. With these three matrix elements, one obtains the tight-binding band structure by diagonalizing the 12×12 Hamiltonian given by Eq. (14) at each $\mathbf{k}$ point.

The tight-binding matrix elements may be estimated from the universal tight-binding parameters of Harrison[35] or from the LMTO theory using potential parameters calculated for Fe_3O_4. The LMTO matrix elements are obtained from the expression

$$t_{dd(\sigma,\pi,\delta)}\approx\Delta_d S_{dd(\sigma,\pi,\delta)} \ , \tag{15a}$$

where Δ_d is the bandwidth parameter. The structure constants S_{dd} fall off as the fifth power of the inverse distance:

$$S_{dd(\sigma,\pi,\delta)}=(-6,4,-1)\times 10(S/R)^5 \ , \tag{15b}$$

where R is the distance between two orbitals and S is the muffin-tin sphere radius. From LMTO theory we obtain the hopping integrals $t_{dd(\sigma,\pi,\delta)}=-0.23$, 0.16, and -0.04 eV, respectively, while by using Harrison's universal parameters we get -0.27, 0.14, and 0.0 eV for the same quantities. It is not surprising that Harrison's universal dd parameters agree with the LMTO matrix elements since the former were in fact derived using parameters from LMTO calculations of Andersen and Jepsen for elemental solids.[36] However, since we retain only the t_{2g} orbitals on the B sublattice and then again only the nearest-neighbor (NN) hopping integrals between these orbitals, the effective values of the tight-binding parameters are expected to change substantially from the above estimates. For instance, the effects of the second nearest neighbors, which are as many as 12 in number and as close as only $\sqrt{3}$ of the NN distance, will be significant even with the R^{-5} scaling of the matrix elements. Thus the effects of the further neighbor interaction will have to be renormalized into our NN matrix elements.

We may obtain the tight-binding matrix elements by fitting the LMTO bands with the tight-binding bands at the Γ point. At this point in the BZ, the Hamiltonian matrix (14) can be diagonalized for the Γ_1, Γ_{12}, and the $\Gamma_{15'}$ states taking advantage of the symmetry of the wave functions. This yields the energy eigenvalues

$$E(\Gamma_1)=\varepsilon_d+\tfrac{3}{2}t_{dd\sigma}-4t_{dd\pi}+\tfrac{1}{2}t_{dd\delta} \ , \tag{16a}$$

$$E(\Gamma_{12})=\varepsilon_d+\tfrac{3}{2}t_{dd\sigma}-t_{dd\pi}-\tfrac{5}{2}t_{dd\delta} \ , \tag{16b}$$

and

$$E(\Gamma_{15'})=\varepsilon_d-\tfrac{3}{2}t_{dd\sigma}+t_{dd\pi}-\tfrac{3}{2}t_{dd\delta} \ . \tag{16c}$$

Here ε_d is the on-site d energy which as mentioned earlier can be put equal to zero by redefining the zero of energy. The energies of the triply degenerate $\Gamma_{25'}$ states may also be easily obtained but since the t_{2g} orbitals span *two* irreducible $\Gamma_{25'}$ representations (see Table V), one has

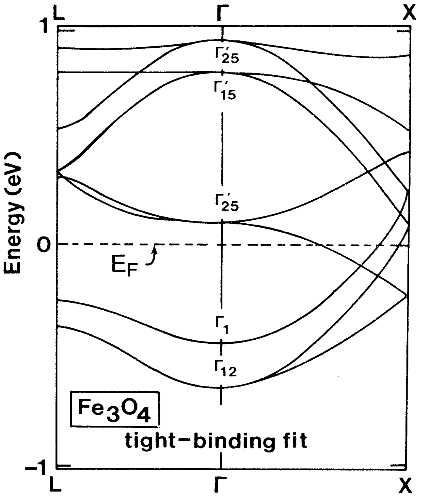

FIG. 7. Nearest-neighbor tight-binding fit to the LMTO minority bands near Fermi energy. The LMTO bands are shown in Fig. 6.

to obtain explicitly the symmetry-adapted partner functions in order to reduce the 6×6 Hamiltonian matrix into 2×2 matrices which can then be easily diagonalized. The three dd matrix elements determined by comparing the LMTO calculated energy eigenvalues with the tight-binding results (16) are $t_{dd\sigma}=-0.406$ eV, $t_{dd\pi}=0.054$ eV, and $t_{dd\delta}=0.122$ eV. With these tight-binding parameters, we calculated the tight-binding bands in the entire BZ to see the quality of the fit. This is shown in Fig. 7, which compares reasonably well with the LMTO bands of Fig. 6. We attempted to obtain a better set of parameters from a least-squares fit of the tight-binding bands with the LMTO bands in the entire BZ. The quality of the fit did not improve significantly, however, indicating that if a better description of the electron bands is needed, one must go beyond the nearest-neighbor interaction and one may perhaps even need to retain interactions of the Fe(B) t_{2g} orbitals with the e_g orbitals on the same atom as well as with orbitals located on other atoms in the crystal. This can be easily accomplished if desired but is not done here since we believe that it is sufficient to retain the NN interaction in the Hamiltonian for the purpose of studying the Verwey transition. The hopping integrals between the individual t_{2g} orbitals can be obtained from the calculated dd parameters in conjunction with the Slater-Koster tables[37] of interatomic matrix elements.

VII. “CONSTRAINED” DENSITY-FUNCTIONAL CALCULATION OF COULOMB PARAMETERS

We now describe the calculation of the on-site and the nearest-neighbor Coulomb parameters for the Fe(B) site. The “constrained” density-functional method is a simple but useful extension of the density-functional theory (DFT). Quite early on, Gunnarsson and Lundqvist[38] showed that in the DFT, in addition to the true ground state the lowest-energy state of each symmetry can be calculated by constraining the symmetry of the ground state. Subsequently Dederichs and co-workers[39] worked out a formalism for calculation of the lowest energy with a more general constraint and successfully applied the method to the calculation of the Coulomb energies for cerium impurities in metals. Here we use this method to calculate the necessary Coulomb interaction parameters. In the “constrained” DFT, the total energy functional is minimized as in the DFT except that now the minimization is performed subject to the constraint that the number of electrons of a particular symmetry within a certain volume Ω be fixed. In our case we will constrain the number of d electrons on the Fe site, i.e., the number of d electrons within the Fe muffin-tin sphere. The constraint is incorporated into the DFT by using the Lagrange multiplier technique so that we now need to minimize the functional $F(n(r),n_d)$:

$$F(\{n(r)\},n_d)=E\{n(r)\}+\lambda\left[\int_\Omega d^3r\,n_d(r)-n_d\right], \tag{17}$$

where λ is the Lagrange multiplier and the total number of d electrons within the volume Ω is constrained to have the value n_d. Minimization of (17) with respect to $n(r)$ leads to the Kohn-Sham local-density equations except that the Lagrange multiplier λ appears as an extra potential to be added to the potentials seen by the electron of the particular symmetry within the volume Ω. Denoting the minimized energy by $E(n_d)$ one gets, from the Hellmann-Feynman theorem,

$$\begin{aligned}\Delta E(n_d^0+\Delta n_d)&\equiv E(n_d^0+\Delta n_d)-E(n_d^0)\\&=-\int_{n_d^0}^{n_d^0+\Delta n_d}dn_d\,\lambda(n_d)\end{aligned} \tag{18}$$

which expresses the increase in energy in terms of the Lagrange multiplier $\lambda(n_d)$ if the ground state is constrained to have Δn_d number of extra electrons on top of the unconstrained value of n_d^0. Now expanding the on-site energy on the atom to second order in n_d, we have

$$E(n_d)=\varepsilon_d n_d+\tfrac{1}{2}Un_d(n_d-1)\ . \tag{19}$$

From (19) the on-site Coulomb energy is given by

$$\begin{aligned}U&=E(n_d^0+1)+E(n_d^0-1)-2E(n_d^0)\\&=\Delta E(n_d^0+1)+\Delta E(n_d^0-1)\ .\end{aligned} \tag{20}$$

If we assume that the Lagrange multiplier $\lambda(n_d)$ is proportional to the difference of n_d from its unconstrained value, i.e., $\lambda(n_d)=-\text{const}\times(n_d-n_d^0)$, we find from Eqs. (18) and (20) that U in fact is equal to the slope of $\lambda(n_d)$. However, this assumption is not necessary in the calculation of U and in general Eq. (20) is used.

In magnetite the relevant atom is the B-site iron atom. It is therefore instructive to present results of our calculation for the isolated Fe atom before we discuss the results for the atom in the crystal. In Table VI we summarize the results of our “constrained” DFT calculations for the isolated Fe atom and compare them to the experimental values. For a certain atomic configuration, e.g., d^5s^2, etc., the atom can exist in many symmetry states; the experimental values quoted in Table VI are obtained by us-

TABLE VI. Results of constrained local-density calculations for the Fe atom.

Quantity	Definition	Expt.[a] (eV)	Present calculations (eV) LDA	LSDA
U_d^s	$E(d^7)+E(d^5s^2)-2E(d^6s)$	3.12	3.35	4.00
U_d^0	$E(d^6s^2)+E(d^4s^2)-2E(d^5s^2)$		15.75	20.07
U_s^0	$E(d^6s^2)+E(d^6)-2E(d^6s)$	8.28	7.51	8.93
$I(1)$[b]	$E(d^6s)-E(d^6s^2)$	7.9	9.39	8.58
$I(2)$[b]	$E(d^6)-E(d^6s^1)$	16.18	16.89	17.52
Δ_{sd}	$E(d^7s)-E(d^6s^2)$	0.86	-0.77	0.35

[a] Reference 40.

[b] $I(1)$ is the first ionization potential, $I(2)$ is the second ionization potential, Δ_{sd} is the *s*-*d* promotion energy.

ing the state with the minimum energy. As seen from the table, the calculated values differ from the experiment typically by ~ 1 eV, an uncertainty we may anticipate in the solid as well. Furthermore, since we might expect that in the solid the on-site U would be bracketed by the screened and the unscreened values in the atom, U_d^s and U_d^0, respectively, from the atomic calculations we should expect $3.1 \lesssim U \lesssim 20$ eV.

There is an additional point that needs to be discussed. Ideally one would like to apply the constraint to a single atom in the solid while the rest of the solid serves as the background. This was the approach followed by Dederichs *et al.* in their original paper using the Green's-function formalism. However, from a computational point of view, it is much simpler to perform supercell calculations with the constraint applied to a periodic array of atoms. This is necessary especially for solids with a large number of atoms in the unit cell in order to keep the computations manageable. Such supercell techniques have been successfully used to calculate Coulomb parameters in earlier work.[41] In magnetite, the unit cell is quite large with a total of 14 atoms including four Fe(B) atoms. In our calculation of U, we applied the constraint to one of these four atoms. Thus the unit cell itself was used as the supercell for calculation of the Coulomb parameters.

In Fig. 8 we show the results of our "constrained" DFT calculation of the Coulomb parameters of the Fe(B) atom. This figure shows in fact the calculation of both the on-site (U) and the nearest-neighbor (U_1) Coulomb parameters. First we focus on the calculation of U. The solid line in Fig. 8(a) shows the variation of the Lagrange multiplier λ as a function of the number of d electrons n_d. $\Delta E(n_d^0+\Delta n_d)$ as obtained by Eq. (18) is shown in Fig. 8(b) from which we obtain the value $U=4.08$ eV using Eq. (20).

We will now discuss the method we used to calculate the nearest-neighbor Coulomb parameter U_1 on the Fe(B) lattice. Consider constraining the occupation of d electrons on two neighboring atoms in the crystal simultaneously. Proceeding as before we now need to minimize, analogously to (17), the functional

$$F[\{n(r)\},n_d^1,n_d^2]=E\{n(r)\}+\lambda_1\left[\int_{\Omega_1} d^3r\, n_d(r)-n_d^1\right] +\lambda_2\left[\int_{\Omega_2} d^3r\, n_d(r)-n_d^2\right], \qquad (21)$$

where the two neighboring sites are constrained to contain, respectively, n_d^1 and n_d^2 numbers of d electrons. Just like the earlier case, minimization of this functional with respect to $\{n(r)\}$ now leads to the Kohn-Sham DFT equations, except that the potentials λ_1 and λ_2 are added to the d-electron potential on the two neighboring atoms. If we now have the further constraint that $n_d^1=n_d^2\equiv n_d$ then from symmetry $\lambda_1=\lambda_2\equiv\lambda$. Analogously to Eq. (19), we now have the expression

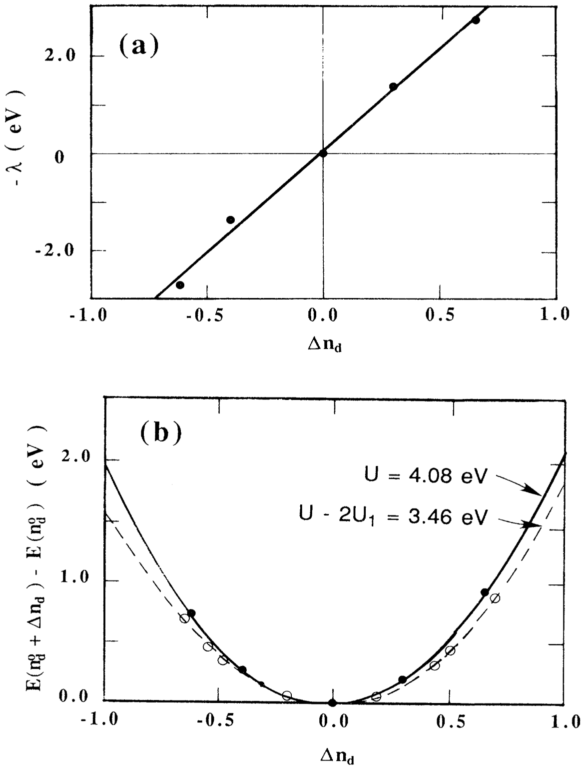

FIG. 8. Results of the "constrained" density-functional calculation of the Coulomb parameters. The solid lines correspond to the case where the d-orbital occupation n_d of only one Fe atom in the unit cell is constrained. The dashed line corresponds to the case where those of two neighboring atoms were constrained as discussed in the text.

$$E(n_d^1,n_d^2)=\varepsilon_d(n_d^1+n_d^2)+\tfrac{1}{2}U[n_d^1(n_d^1-1)+n_d^2(n_d^2-1)] + U_1 n_d^1 n_d^2 \qquad (22)$$

for the energy of a pair of atoms on NN sites with U_1 being the NN Coulomb interaction energy. Equation (22) then gives

$$E(n_d^0+1,n_d^0+1)+E(n_d^0-1,n_d^0-1)-2E(n_d^0,n_d^0) =2U+2U_1 \ . \qquad (23)$$

We then get

$$U+U_1=\left[\int_{n_d^0}^{n_d^0+1}+\int_{n_d^0}^{n_d^0-1}\right]-\lambda(n_d)dn_d \ . \qquad (24)$$

However, since our calculations are supercell calculations where we constrain n_d of two Fe(B) atoms in *each* unit cell, the connectivity of the B sublattice (see Fig. 9) is such that we get a factor of 2 in the coefficient of U_1 in (24).

Similarly, one can show that if the constraint on the two neighboring atoms is such that $\Delta n_d^1=-\Delta n_d^2$, then $\lambda_1\approx-\lambda_2\equiv\lambda$, in which case we have

$$U-2U_1=\left[\int_{n_d^0}^{n_d^0+1}+\int_{n_d^0}^{n_d^0-1}\right]-\lambda(n_d)dn_d \ . \qquad (25)$$

In our calculation we constrained the number of d electrons on two neighboring Fe atoms on the B site to be $n_d^0+\Delta n_d$ and $n_d^0-\Delta n_d$, respectively. The result of this calculation is shown by the dashed lines in Fig. 8, from which we get the value $U-2U_1=3.46$ eV.

We now describe an alternative way of calculating U_1, where we constrain the occupation of one Fe(B) atom/cell and examine the on-site one-electron energies of the d orbitals on various atoms as, for instance, given by the band-center energy in the LMTO calculation. The four Fe(B) atoms in the unit cell are now inequivalent. The B sublattice is such that each Fe(B) atom is surrounded by two each of the other three inequivalent Fe(B) atoms (see Fig. 9). The on-site energy on atom 1 is therefore given by

$$\bar{\varepsilon}_d(1)=\varepsilon_d+U(n_d^{(1)}-1)+2U_1(n_d^{(2)}+n_d^{(3)}+n_d^{(4)}) \ , \qquad (26)$$

where $n_d^{(i)}$ is the number of d electrons on the ith atom and the factor of 2 in the last term in (26) comes from taking all nearest neighbors into account. Combining (26) with a similar expression for atom 2, we obtain the equation for the difference in the on-site energies

$$\bar{\varepsilon}_d(1)-\bar{\varepsilon}_d(2)=(U-2U_1)(n_d^{(1)}-n_d^{(2)}) \ . \qquad (27)$$

In the actual calculation, we added the extra potential λ to one of the four Fe(B) atoms in each unit cell and used the LMTO band-center energies as the on-site d energies. Figure 10 shows the variation of the on-site energy difference plotted against the difference in the number of d electrons. As indicated from (27) there is a linear relationship between these two quantities which is followed by our numerical results (see Fig. 10). From the slope we obtain the value $U-2U_1=3.32$ eV which is somewhat less than the value of 3.46 eV obtained from the method of Dederichs *et al.* (Fig. 8). This difference may be taken as a measure of the uncertainty in the methods used. Using the value of $U=4.1$ eV, we then obtain the value of $U_1=0.3-0.4$ eV. These values of the Coulomb parameters as well as the tight-binding parameters for the spin-down band at the Fermi energy are summarized in Table VII.

The retention of the second nearest-neighbor Coulomb interaction U_2 in addition to U_1 in the model Hamiltonian (11) may be important to the stabilization of the long-range order. In fact Ihle and Lorenz[42] working within the one-band model have argued that for the LRO to be stabilized U_2 should be greater than t^3/U_1^2, i.e., $\gtrsim 0.02$ eV estimated from our parameters. Unfortunately we cannot at present calculate U_2 reliably from the "constrained" DFT calculation because the energy differences

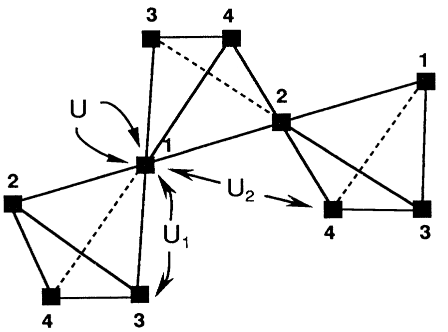

FIG. 9. Connectivity of the B sublattice in the spinel structure. The four B sites forming the basis of the unit cell are numbered one through four. Each site has six nearest neighbors and 12 second nearest neighbors. The on-site and nearest-neighbor Coulomb energies, denoted by U, U_1, and U_2, are schematically shown.

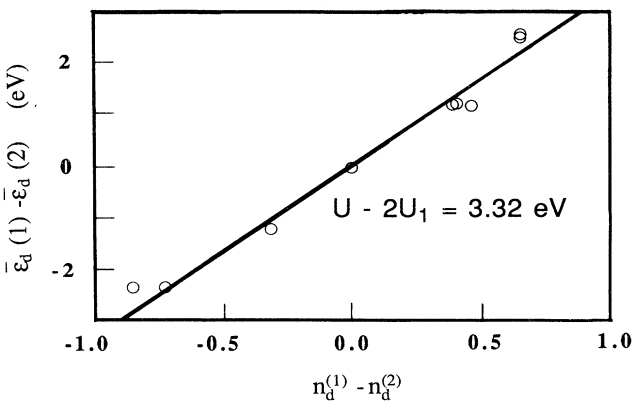

FIG. 10. Calculation of the Coulomb parameter $U-2U_1$ using Eq. (27).

TABLE VII. Summary of the calculated relevant hopping integrals and Coulomb parameters for the Fe(B) site in Fe_3O_4.

Tight-binding hopping integrals	Coulomb parameters
$t_{dd\sigma}=-0.41$ eV	$U=4.1\pm0.5$ eV
$t_{dd\pi}=0.05$ eV	$U_1=0.3-0.4$ eV
$t_{dd\delta}=0.12$ eV	$U_2\lesssim0.05-0.1$ eV
$W=1.55$ eV	
$t=-0.13$ eV	

are too small and, furthermore, the supercell size becomes excessively large. We have in fact neglected it in the calculation of U_1. Now, if we suppose that the Coulomb repulsion scales roughly as the inverse of the distance, $U\sim e^2/\kappa a$, then from the calculated value of U_1 and the ratio of the distances we might estimate $U_2\sim U_1/(3)^{1/2}\sim0.2$ eV. However, for a poor metal like magnetite screening is not expected to be complete by the nearest-neighbor distance in which case we would expect the value of U_2 to be much lower than 0.2 eV. Considering this, a value of $U_2\lesssim0.05-0.1$ eV seems to be a reasonable estimate.

VIII. CONCLUDING REMARKS

From the results of our LSDA calculations it emerges that the relevant electron orbitals responsible for conduction are the Fe t_{2g} orbitals on the B sublattice, since these orbitals exist at the Fermi energy. Furthermore, since only minority spin bands occur at the Fermi energy, the majority spin states are unavailable for transport properties. Our calculations therefore provide direct support to the earlier models of conduction where the charge carriers move on the B sublattice in a spinless band. However, in contrast to the earlier models such as the Cullen-Callen model our results indicate that the electrons move in the triplet band formed out of the t_{2g} orbitals on the B sublattice. Furthermore, there is exactly one-half electron per Fe(B) atom occupying the Fe(B) t_{2g} bands. These are the so-called "extra" electrons that order in the ground state to minimize the Coulomb interaction between them. This is equivalent to ordering of Fe^{2+} and Fe^{3+} ions on the B sublattice.

Since there is only half an electron per atom in the B sublattice and since the on-site Coulomb U of 4.1 eV is rather large, this effectively eliminates double occupancy of the atoms to a very good approximation. This leads to the simplification that in the three-band model Hamiltonian it is reasonable to omit the on-site Coulomb term ($U=\infty$ limit). Thus the most important relevant Coulomb parameter is the NN Coulomb repulsion term U_1.

To our knowledge there exists no theoretical work on the three-band spinless model Hamiltonian. On the other hand, there exists a wealth of literature on the one-band Cullen-Callen model:

$$H=t\sum_{\langle ij\rangle}a_i^\dagger a_j+U_1\sum_{\langle ij\rangle}n_in_j\ , \tag{28}$$

on the basis of which the nature of the Verwey transition has been examined in earlier works. In (28) the angular brackets indicate that only nearest-neighbor interactions are to be retained. To make a connection with the Cullen-Callen model one may calculate an effective one-band hopping integral t from our calculated parameters by the following average:

$$t^2\equiv\sum_{\mu=1}^{3}|t_{xy,\mu}|^2 \tag{29}$$

which represents the average hopping matrix element from one of the t_{2g} orbitals (say xy) of a certain atom to its nearest neighbor whose orbitals are denoted by $\mu=xy$, yz, or zx. Using (29), we get an effective hopping integral $t=-0.13$ eV. Another way to estimate an average t would be to divide the calculated bandwidth W by two times the number of nearest-neighbor z, $t\sim w/2z$, which also gives a value of $|t|\sim0.13$ eV. With the value of $U_1=0.3-0.4$ eV, we therefore get $U_1/t\sim2-3$.

In their original paper Cullen and Callen,[34] based on a Hartree-Fock analysis, had estimated that for the value of $U_1/t\gtrsim2.5$ the Coulomb term is strong enough to produce an ordering of the "extra" electrons. The model is in fact exactly solvable in one dimension[43] which shows a Coulomb gap for $U_1/t>2$. Ihle and Lorenz[42] argued that for the spinel B sublattice of magnetite a Coulomb gap would form for $U_1/t\gtrsim3$. Since the calculated parameters are in this range of values, this indicates that an electronic Hamiltonian may be enough to treat the Verwey transition. We are currently studying the properties of the three-band model with regard to the Verwey transition.

In conclusion, we have examined the electronic band structure of magnetite in the spinel structure from a local-density calculation and have suggested a three-band model Hamiltonian for the description of the Verwey transition. A study of the proposed three-band Hamiltonian seems to be necessary for the understanding of the Verwey transition.

ACKNOWLEDGMENTS

The present work was supported in part by a Grant from the Weldon Spring Foundation of the University of Missouri. Numerical computations were performed at the Pittsburgh Supercomputing Center at Pittsburgh and at the National Center for Supercomputing Applications at Urbana-Champaign.

---

[1] N. F. Mott, *Metal-Insulator Transitions* (Taylor & Francis, London, 1964).

[2] For a more recent overview of the current understanding on the Verwey metal-insulator transition in magnetite, see the papers presented at the Cavendish Meeting, September 1979: Philos. Mag. **42**, 327 (1980).

[3] E. J. W. Verwey, Nature **144**, 327 (1939); E. J. W. Verwey and P. W. Haayman, Physica **8**, 979 (1941); E. J. W. Verwey, P.

W. Haayman, and F. C. Romeijn, J. Chem. Phys. **15**, 181 (1947).

[4] P. W. Anderson, Phys. Rev. **102**, 1008 (1956).

[5] M. Matsui, S. Todo, and S. Chikazumi, J. Phys. Soc. Jpn. **42**, 1517 (1977).

[6] M. Iizumi, T. F. Koetzle, G. Shirane, S. Chikazumi, M. Matsui, and S. Todo, Acta Crystallogr. **38**, 2121 (1982); S. Iida, Philos. Mag. **42**, 349 (1980); J. Yoshida and S. Iida, J. Phys. Soc. Jpn. **42**, 236 (1977).

[7] An account of the history of magnetite is given by D. C. Mattis, *The Theory of Magnetism* (Springer-Verlag, Berlin, 1988), Vol. I.

[8] J. R. Cullen and E. R. Callen, J. Appl. Phys. **41**, 879 (1970).

[9] E. I. Terukov, W. Reichelt, D. Ihle, and H. Oppermann, Phys. Status Solidi B **95**, 491 (1979).

[10] Y. Yamada, Philos. Mag. B **42**, 377 (1980).

[11] B. K. Chakraverty, Solid State Commun. **15**, 1271 (1974).

[12] N. F. Mott, Festkörperprobleme **19**, 331 (1979); also in Ref. 2.

[13] Site indices refer to the tables contained in *International Tables for X-ray Crystallography,* edited by N. F. M. Henry and K. Lonsdale (Kynoch, Birmingham, England, 1969), Vol. 1.

[14] L. Néel, Ann. Phys. (Leipzig) **3**, 137 (1948).

[15] C. G. Shull, F. O. Wollan, and W. C. Koehler, Phys. Rev. **84**, 912 (1951).

[16] O. K. Andersen, Phys. Rev. B **12**, 3060 (1975); H. L. Skriver, *The LMTO Method* (Springer, New York, 1983).

[17] U. von Barth and L. Hedin, J. Phys. C **5**, 1629 (1972).

[18] E. C. Stoner, Proc. R. Soc. London, Ser. A **169**, 339 (1939).

[19] S. H. Vosko and J. P. Perdew, Can. J. Phys. **53**, 1385 (1975).

[20] O. Gunnarsson, J. Phys. F **6**, 587 (1976).

[21] J. F. Janak, Phys. Rev. B **16**, 255 (1977).

[22] G. L. Krasko, Phys. Rev. B **36**, 8565 (1987).

[23] O. K. Andersen, O. Jepsen, and D. Glötzel, in *Highlights in Condensed Matter Theory,* edited by F. Bassani, F. Fumi, and N. Tosi (North-Holland, Amsterdam, 1985), and references therein.

[24] U. K. Poulsen, J. Kollár, and O. K. Andersen, J. Phys. F **6**, L241 (1976).

[25] F. Bloch, Z. Phys. **57**, 545 (1929).

[26] A. Yanase and K. Siratori, J. Phys. Soc. Jpn. **53**, 312 (1984).

[27] S. G. Bishop and P. C. Kemeny, Solid State Commun. **15**, 1877 (1974).

[28] E. W. Gorter, Proc. IRE **43**, 245 (1955), cited by S. Chikazumi and S. H. Charap, *Physics of Magnetism* (Krieger, Malabar, FL, 1986).

[29] Z. Kakol and J. M. Honig, Phys. Rev. B **40**, 9090 (1989).

[30] V. C. Rakhecha and N. S. Satya Murthy, J. Phys. C **11**, 4389 (1978).

[31] See, for example, J. B. Goodenough, in *Progress in Solid State Chemistry,* edited by H. Reiss (Pergamon, New York, 1971), Vol. 5, p. 145.

[32] S. F. Alvarado, W. Eib, F. Meier, D. T. Pierce, K. Sattler, H. C. Siegmann, and J. P. Remeika, Phys. Rev. Lett. **34**, 319 (1975).

[33] S. Satpathy and R. M. Martin, Phys. Rev. **36**, 7269 (1987); S. Massidda, J. Yu, and A. J. Freeman, *ibid.* **38**, 11 352 (1988).

[34] J. R. Cullen and E. R. Callen, Phys. Rev. B **7**, 397 (1973).

[35] W. A. Harrison, *Electronic Structure and the Properties of Solids* (Freeman, San Francisco, 1979).

[36] O. K. Andersen and O. Jepsen, Physica B+C **91B**, 317 (1977); see W. A. Harrison, *Electronic Structure and the Properties of Solids* (Ref. 35), p. 487.

[37] J. C. Slater and G. F. Koster, Phys. Rev. **94**, 1498 (1954).

[38] O. Gunnarsson and B. I. Lundqvist, Phys. Rev. B **13**, 4274 (1976).

[39] P. H. Dederichs, S. Blügel, R. Zeller, and H. Akai, Phys. Rev. Lett. **53**, 2512 (1984).

[40] C. E. Moore, *Atomic Energy Levels,* Natl. Bur. Stand. (U.S.) Circ. No. 467 (U.S. GPO, Washington, D.C., 1952).

[41] A. K. McMahan, R. M. Martin, and S. Satpathy, Phys. Rev. B **38**, 6650 (1988).

[42] D. Ihle and B. Lorenz, Philos. Mag. **42**, 337 (1980).

[43] J. Des Cloizeaux, J. Math. Phys. **7**, 2136 (1966); M. Fowler, Phys. Rev. B **17**, 2989 (1978).